

Air Force Institute of Technology

**AFIT Scholar**

---

Faculty Publications

---

5-2017

## Kinetics of High Pressure Argon-helium Pulsed Gas Discharge

Daniel J. Emmons

*Air Force Institute of Technology*

David E. Weeks

*Air Force Institute of Technology*

Follow this and additional works at: <https://scholar.afit.edu/facpub>



Part of the [Plasma and Beam Physics Commons](#)

---


### Recommended Citation

Emmons, D. J., & Weeks, D. E. (2017). Kinetics of high pressure argon-helium pulsed gas discharge. *Journal of Applied Physics*, 121(20), 203301. <https://doi.org/10.1063/1.4983678>

This Article is brought to you for free and open access by AFIT Scholar. It has been accepted for inclusion in Faculty Publications by an authorized administrator of AFIT Scholar. For more information, please contact [richard.mansfield@afit.edu](mailto:richard.mansfield@afit.edu).

RESEARCH ARTICLE | MAY 22 2017

# Kinetics of high pressure argon-helium pulsed gas discharge

D. J. Emmons; D. E. Weeks 



*Journal of Applied Physics* 121, 203301 (2017)

<https://doi.org/10.1063/1.4983678>



View Online



Export Citation

CrossMark

## AIP Advances

Why Publish With Us?

-  **25 DAYS**  
average time to 1st decision
-  **740+ DOWNLOADS**  
average per article
-  **INCLUSIVE**  
scope

[Learn More](#)



# Kinetics of high pressure argon-helium pulsed gas discharge

D. J. Emmons<sup>a)</sup> and D. E. Weeks

*Department of Physics, Air Force Institute of Technology, Wright-Patterson AFB, Ohio 45433, USA*

(Received 16 January 2017; accepted 5 May 2017; published online 22 May 2017)

Simulations of a pulsed direct current discharge are performed for a 7% argon in helium mixture at a pressure of 270 Torr using both zero- and one-dimensional models. Kinetics of species relevant to the operation of an optically pumped rare-gas laser are analyzed throughout the pulse duration to identify key reaction pathways. Time dependent densities, electron temperatures, current densities, and reduced electric fields in the positive column are analyzed over a single 20  $\mu$ s pulse, showing temporal agreement between the two models. Through the use of a robust reaction rate package, radiation trapping is determined to play a key role in reducing  $Ar(1s_5)$  metastable loss rates through the reaction sequence  $Ar(1s_5) + e^- \rightarrow Ar(1s_4) + e^-$  followed by  $Ar(1s_4) \rightarrow Ar + \hbar\omega$ . Collisions with He are observed to be responsible for  $Ar(2p_9)$  mixing, with nearly equal rates to  $Ar(2p_{10})$  and  $Ar(2p_8)$ . Additionally, dissociative recombination of  $Ar_2^+$  is determined to be the dominant electron loss mechanism for the simulated discharge conditions and cavity size.

[<http://dx.doi.org/10.1063/1.4983678>]

## I. INTRODUCTION

An optically pumped rare-gas laser (OPRGL), as demonstrated by Han *et al.*,<sup>1</sup> uses a diode laser to pump metastable  $Rg(1s_5)$  atoms generated in a gas discharge to the  $Rg(2p_9)$  level (using Paschen notation). At atmospheric pressures, rapid collisional transfer from  $Rg(2p_9)$  to  $Rg(2p_{10})$  allows for a population inversion and subsequent lasing to  $Rg(1s_5)$ , as displayed in Fig. 1. Diode laser absorption and hence optical gain are dependent on  $Rg(1s_5)$  densities.<sup>2,3</sup> Output laser intensities above 100 W/cm<sup>2</sup> may be possible with a uniform volume of metastable densities on the order of 10<sup>13</sup> cm<sup>-3</sup>.<sup>4</sup> Due to the broad line widths of diode lasers, atmospheric pressures are required to broaden the absorption line width for efficient pump laser absorption. Additionally, the non-adiabatic transition rate from  $Rg(2p_9)$  to  $Rg(2p_{10})$ , responsible for establishing a population inversion, is enhanced at elevated pressures. Pulsed discharges are able to maintain stability at atmospheric pressures due to a reduction in thermal instabilities caused by the down time in-between pulses.<sup>5</sup> Additionally, for the same averaged power, the average plasma density of a pulsed system is greater than a steady-state direct current (DC) discharge as a result of a reduction in electron temperature in-between pulses.<sup>6,7</sup>

Han *et al.*<sup>1</sup> demonstrated the use of a pulsed DC circuit to produce an OPRGL in an Ar-He mixture at atmospheric pressures. Voltages in the range of 1000–2000 V were used for microsecond pulses across a parallel plate geometry. Metastable densities, measured through pump laser absorption, indicated a decay to half the peak value approximately 7  $\mu$ s after pulse initiation.

Previously, a kinetic study of an OPRGL using a mixture of Ar and He at atmospheric pressures concluded that a mixture of approximately 1% Ar in He results in the largest total efficiency (defined as the output power divided by the sum of discharge and pump powers).<sup>3</sup> The kinetic study

observed that an increase in Ar-fraction increases the production of  $Ar(1s_5)$  and also results in a larger collision relaxation rate from the  $Ar(2p)$  manifold down to the  $Ar(1s_5)$  manifold in addition to an increase in the  $Ar(1s_5)$  loss rate through excimer formation. A separate kinetic analysis studied OPRGL performance over a variety of metastable densities, showing the possibility of kilowatt laser powers for an OPRGL system with  $Ar(1s_5)$  densities on the order of 10<sup>13</sup> cm<sup>-3</sup> and pump laser intensities in the 2–5 kW/cm<sup>2</sup> range.<sup>8</sup> An experimental and computational analysis of microwave resonator-driven microplasmas at various Ar-He mixtures and atmospheric pressures found that an Ar-fraction near 5% produces the largest metastable densities.<sup>9</sup> Metastable densities on the order of 10<sup>13</sup> cm<sup>-3</sup> were measured for the microplasmas at a pressure of 100 Torr, with a decrease in  $Ar(1s_5)$  density as the pressure increased.

More recently, Han *et al.*<sup>10</sup> performed an Ar-He pulsed DC discharge experiment at a pressure of 270 Torr and a mixture of 7% Ar in He, with 2.5 cm  $\times$  2.5 cm stainless steel electrodes separated by 0.5 cm. Metastable  $Ar(1s_5)$  densities were measured via transient laser absorption spectroscopy from a custom made diode laser tuned to the  $Ar(1s_5) + \hbar\omega \rightarrow Ar(2p_9)$  transition. Plasma fluorescence due to the  $Ar(2p_{10}) \rightarrow Ar(1s_5) + \hbar\omega$  transition was also measured, providing a proxy for  $Ar(2p_{10})$  density over time.

In this paper, we present a reaction rate package designed to track the concentrations of the various species in a pulsed Ar-He discharge that are important in the operation of OPRGL systems. This reaction rate package is used to perform zero-dimensional and one-dimensional simulations of a pulsed DC discharge over a single pulse. Discharge kinetics are investigated, and key reaction pathways are identified. Previously, zero-dimensional simulations using the rate package presented here were compared with experimental pulsed discharge data, where it was determined that the radiation trapping plays a key role in post-pulse metastable lifetimes.<sup>10</sup> Additionally, the inclusion of a He quenching reaction, which may be a proxy for quenching due to

<sup>a)</sup>Electronic mail: daniel.emmons@afit.edu

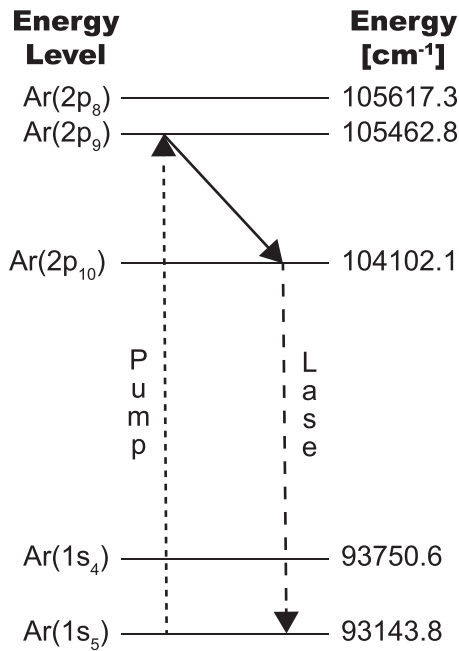


FIG. 1. A diagram of energy levels pertinent to an optically pumped rare-gas laser with Ar as the rare-gas. Optical pumping from  $Ar(1s_5)$  to  $Ar(2p_9)$  is followed by a non-adiabatic transition to  $Ar(2p_{10})$  and subsequent lasing to  $Ar(1s_4)$ . Lasing to  $Ar(1s_4)$  is also possible, and  $Ar(2p_8)$  is included due to its proximity to the pumping level  $Ar(2p_9)$ .

impurities, increased the qualitative agreement between simulations and measured absorption.

## II. MODELS

A list of the species used to analyze OPRGL kinetics for both the zero and one-dimensional models is displayed in Table I. Excited Ar species  $Ar(1s_5)$ ,  $Ar(2p_{10})$ , and  $Ar(2p_9)$  are included due to their central role in OPRGL operation. Additionally,  $Ar(1s_4)$  and  $Ar(2p_8)$  are retained because of their proximity to  $Ar(1s_5)$  and  $Ar(2p_8)$ , respectively. The remaining  $Ar(1s)$  and  $Ar(2p)$  species are ignored to limit the reaction rate package complexity. An additional excited

TABLE I. A list of Ar-He species relevant to the operation of an optically pumped rare-gas laser and their corresponding energy levels. Macro-species energies are represented by the lowest energy level for the collection of species represented by the macro-species.

Species	Energy (eV)
$Ar_2^*$	11.06
$Ar(1s_5)$	11.55
$Ar(1s_4)$	11.62
$Ar(2p_{10})$	12.91
$Ar(2p_9)$	13.08
$Ar(2p_8)$	13.10
$Ar(h.l.)$	13.85
$Ar_2^+$	14.50
$HeAr^+$	15.74
$Ar^+$	15.76
$He_2^*$	17.97
$He^*$	19.80
$He_2^+$	22.23
$He^+$	24.58

species  $Ar(h.l.)$  is used as a macro-species, encompassing all electronic levels of Ar above  $Ar(3d_{12})$ .

Excited levels of He are represented by the macro-species  $He^*$ . At atmospheric pressures, dimers play an important kinetic role requiring the macro-species  $He_2^*$  and  $Ar_2^*$ , which represent all He and Ar dimer energy levels. Finally, the ion species  $Ar^+$ ,  $Ar_2^+$ ,  $He^+$ ,  $He_2^+$ , and  $HeAr^+$  are included. The energy used to represent the macro-species is the lowest energy level for the collection of species represented by the macro-species. Dimer energies of 11.06 and 17.97 eV are used for  $Ar_2^*$  and  $He_2^*$ , respectively.<sup>11</sup> A list of reactions for the species of interest is displayed in Table II. This reaction rate package includes electron impact, recombination, two-heavy-body, three-heavy-body, and radiative rate coefficients. With the exception of a few assumptions listed in the footnotes of Table II, all rate coefficients are taken directly from the literature with no adjustment.

Electron impact rate coefficients are calculated using BOLSIG+, which uses a two-term approximation to solve the Boltzmann equation.<sup>12</sup> After the non-Maxwellian electron energy distribution function (EEDF) is calculated, rate coefficients for electron impact collisions are computed by

$$k_i = \sqrt{\frac{2qe}{m_e}} \int_0^\infty \epsilon \sigma_i(\epsilon) f(\epsilon) d\epsilon, \quad (1)$$

where  $k_i$  is the rate coefficient for the  $i^{\text{th}}$  reaction,  $\epsilon$  is the electron energy,  $\sigma_i(\epsilon)$  is the cross section for the  $i^{\text{th}}$  reaction, and  $f(\epsilon)$  is the EEDF. The main driver of the EEDF is the reduced electric field,  $E/N$ , where  $N$  is the neutral gas density. Reduced electric fields are calculated over time to provide an updated EEDF for the current discharge conditions. Transport parameters, including electron mobility and diffusion coefficients, are also calculated from the EEDF.

Metastable quenching rates due to collisions with neutrals via  $Ar(1s_5) + M \rightarrow Ar + M$  play an important role in the decay rates after breakdown. However, these reactions may in part be a proxy for collisions with impurities, allowing the quenching from impurities to be taken into account (see Stefanović *et al.*<sup>42</sup> for a discussion on quenching due to impurities). Radiation trapping<sup>43</sup> for the  $Ar(1s_4) \rightarrow Ar + \hbar\omega$  transition is taken into account, using an effective A-coefficient of  $5.6 \times 10^5 \text{ s}^{-1}$  reported by Han and Heaven.<sup>30</sup> This radiation trapping term was found to be vital to the post-pulse metastable decay rates due to the loss pathway through  $Ar(1s_4) \rightarrow Ar + \hbar\omega$  radiation.

### A. Zero-dimensional model

The zero-dimensional model, implemented through ZDPlasKin (Zero-Dimensional Plasma Kinetics), models the positive column of a glow discharge by numerically integrating the system of reaction rate equations over time, accounting for changes in discharge parameters and species concentrations.<sup>44</sup> Due to the electron impact rate coefficient and mobility dependence on  $E/N$ , the positive column  $E/N$  must be calculated at each time step to provide an input to BOLSIG+, which provides an updated set of electron impact

rate coefficients and electron mobility. A simple method for calculating the  $E/N$  over time caused by a voltage drop across a ballast resistor is described in Eismann<sup>45</sup> and is used as a basis for this analysis.

In addition to the chemical reactions listed in Table II, ambipolar diffusion loss is calculated for the zero-dimensional model, with the ambipolar loss frequency,  $\nu_a$ , provided by

$$\nu_a = \frac{D_a}{\Lambda^2} \approx \frac{\mu_+ T_e}{\Lambda^2}, \quad (2)$$

where  $D_a$  is the ambipolar diffusion coefficient,  $\Lambda \approx 1.5$  mm is the characteristic length of the cavity,  $\mu_+$  is the ion mobility, and  $T_e$  is the electron temperature in eV.<sup>5</sup> Ion mobilities are calculated using Blanc's law,<sup>46</sup> assuming that  $Ar_2^+$  and  $HeAr^+$  mobilities are equal to the mobility of  $Ar^+$  in Ar-He

TABLE II. A list of reaction rate coefficients used to model high pressure Ar-He pulsed gas discharge kinetics for species relevant to the operation of an optically pumped rare-gas laser.  $T_e$  is in eV and  $T_{gas}$  is in K. A discussion of the BOLSIG+ calculated rate coefficients can be found in Hagelaar and Pitchford.<sup>12</sup>

Reaction	Rate coefficient $\left[ \frac{1}{s}, \frac{cm^2}{s}, \text{ or } \frac{cm^6}{s} \right]$	References
<b>Electron impact</b>		
$Ar + e^- \rightarrow Ar^+ + e^- + e^-$	BOLSIG+	13
$Ar(1s_5) + e^- \rightarrow Ar^+ + e^- + e^-$	BOLSIG+	13
$Ar(1s_4) + e^- \rightarrow Ar^+ + e^- + e^-$	BOLSIG+	13 <sup>a</sup>
$Ar(2p_{10}) + e^- \rightarrow Ar^+ + e^- + e^-$	BOLSIG+	13 <sup>a</sup>
$Ar(2p_9) + e^- \rightarrow Ar^+ + e^- + e^-$	BOLSIG+	13 <sup>a</sup>
$Ar(2p_8) + e^- \rightarrow Ar^+ + e^- + e^-$	BOLSIG+	13 <sup>a</sup>
$Ar(h.l.) + e^- \rightarrow Ar^+ + e^- + e^-$	BOLSIG+	13 <sup>a</sup>
$Ar + e^- \leftrightarrow Ar(1s_5) + e^-$	BOLSIG+	14
$Ar + e^- \leftrightarrow Ar(1s_4) + e^-$	BOLSIG+	14
$Ar + e^- \leftrightarrow Ar(2p_{10}) + e^-$	BOLSIG+	14
$Ar + e^- \leftrightarrow Ar(2p_9) + e^-$	BOLSIG+	14
$Ar + e^- \leftrightarrow Ar(2p_8) + e^-$	BOLSIG+	14
$Ar + e^- \leftrightarrow Ar(h.l.) + e^-$	BOLSIG+	14 <sup>b</sup>
$Ar(2p_{10}) + e^- \leftrightarrow Ar(2p_9) + e^-$	BOLSIG+	15
$Ar(2p_{10}) + e^- \leftrightarrow Ar(2p_8) + e^-$	BOLSIG+	15
$Ar(2p_{10}) + e^- \leftrightarrow Ar(h.l.) + e^-$	BOLSIG+	14 <sup>c</sup>
$Ar(2p_9) + e^- \leftrightarrow Ar(2p_8) + e^-$	BOLSIG+	15 <sup>d</sup>
$Ar(2p_9) + e^- \leftrightarrow Ar(h.l.) + e^-$	BOLSIG+	14 <sup>c</sup>
$Ar(2p_8) + e^- \leftrightarrow Ar(h.l.) + e^-$	BOLSIG+	14 <sup>c</sup>
$Ar(1s_4) + e^- \leftrightarrow Ar(2p_{10}) + e^-$	BOLSIG+	15
$Ar(1s_4) + e^- \leftrightarrow Ar(2p_9) + e^-$	BOLSIG+	15
$Ar(1s_4) + e^- \leftrightarrow Ar(2p_8) + e^-$	BOLSIG+	15
$Ar(1s_4) + e^- \leftrightarrow Ar(h.l.) + e^-$	BOLSIG+	14 <sup>c</sup>
$Ar(1s_5) + e^- \leftrightarrow Ar(1s_4) + e^-$	BOLSIG+	15
$Ar(1s_5) + e^- \leftrightarrow Ar(2p_{10}) + e^-$	BOLSIG+	15
$Ar(1s_5) + e^- \leftrightarrow Ar(2p_9) + e^-$	BOLSIG+	15
$Ar(1s_5) + e^- \leftrightarrow Ar(2p_8) + e^-$	BOLSIG+	15
$Ar(1s_5) + e^- \leftrightarrow Ar(h.l.) + e^-$	BOLSIG+	14 <sup>c</sup>
$He + e^- \rightarrow He^+ + e^- + e^-$	BOLSIG+	13 and 16
$He + e^- \leftrightarrow He^* + e^-$	BOLSIG+	13 and 17
$He^* + e^- \rightarrow He^+ + e^- + e^-$	BOLSIG+	13 and 17
$Ar_2^+ + e^- \rightarrow Ar_2^+ + e^- + e^-$	BOLSIG+	18
$Ar_2^+ + e^- \rightarrow Ar + Ar + e^-$	BOLSIG+	19
$Ar_2^+ + e^- \rightarrow Ar(1s_5) + Ar + e^-$	$1.00 \times 10^{-8} \exp(-1.00/T_e)$	20
$Ar_2^+ + e^- \rightarrow Ar^+ + Ar + e^-$	$1.36 \times 10^{-6} \exp(-2.09/T_e)$	21
$He_2^+ + e^- \rightarrow He_2^+ + e^- + e^-$	$9.75 \times 10^{-10} T_e^{0.71} \exp(-3.40/T_e)$	22
$He_2^+ + e^- \rightarrow He + He + e^-$	$3.80 \times 10^{-9}$	23
$He_2^+ + e^- \rightarrow He^+ + He + e^-$	$1.06 \times 10^{-7} T_e^{-3} \exp(-9.97/T_e)$	24
<b>Recombination</b>		
$Ar^+ + e^- + e^- \rightarrow Ar(h.l.) + e^-$	$7.20 \times 10^{-27} T_e^{-4.5}$	25
$Ar^+ + e^- + M \rightarrow Ar(h.l.) + M$	$1.10 \times 10^{-30} T_e^{-2.5}$	26
$He^+ + e^- + e^- \rightarrow He^* + e^-$	$5.10 \times 10^{-27} T_e^{-4.5}$	26
$He^+ + e^- + M \rightarrow He^* + M$	$1.10 \times 10^{-30} T_e^{-2.5}$	26
$He_2^+ + e^- \rightarrow He^* + He$	$5.00 \times 10^{-9} T_e^{-0.5}$	25
$Ar_2^+ + e^- \rightarrow Ar(h.l.) + Ar$	$7.34 \times 10^{-8} T_e^{-0.67}$	27
$HeAr^+ + e^- \rightarrow Ar(h.l.) + He$	$7.34 \times 10^{-9} T_e^{-0.67}$	25 <sup>c</sup>

TABLE II. (Continued.)

Reaction	Rate coefficient	References
	$\frac{\text{l}}{\text{s}}$ , $\frac{\text{cm}^3}{\text{s}}$ , or $\frac{\text{cm}^6}{\text{s}}$	
<b>Two-heavy-body</b>		
$\text{Ar}(1s_5) + \text{Ar} \rightarrow \text{Ar} + \text{Ar}$	$2.30 \times 10^{-15}$	28
$\text{Ar}(1s_5) + \text{He} \rightarrow \text{Ar} + \text{He}$	$1.60 \times 10^{-14}$	29
$\text{Ar}(1s_5) + \text{Ar} \leftrightarrow \text{Ar}(1s_4) + \text{Ar}$	$2.10 \times 10^{-15}$	3
$\text{Ar}(1s_4) + \text{He} \leftrightarrow \text{Ar}(1s_5) + \text{He}$	$1.00 \times 10^{-13}$	30 <sup>f</sup>
$\text{Ar}(2p_{10}) + \text{Ar} \leftrightarrow \text{Ar}(1s) + \text{Ar}$	$1.50 \times 10^{-11} \sqrt{T_{\text{gas}}/300}$	31 <sup>g</sup>
$\text{Ar}(2p_{10}) + \text{He} \leftrightarrow \text{Ar}(1s) + \text{He}$	$0.50 \times 10^{-13} \sqrt{T_{\text{gas}}/300}$	30 <sup>g,h</sup>
$\text{Ar}(2p_9) + \text{Ar} \leftrightarrow \text{Ar}(1s) + \text{Ar}$	$3.00 \times 10^{-11} \sqrt{T_{\text{gas}}/300}$	31 <sup>g</sup>
$\text{Ar}(2p_9) + \text{He} \leftrightarrow \text{Ar}(1s) + \text{He}$	$0.20 \times 10^{-11} \sqrt{T_{\text{gas}}/300}$	30 <sup>g,h</sup>
$\text{Ar}(2p_8) + \text{Ar} \leftrightarrow \text{Ar}(1s) + \text{Ar}$	$4.00 \times 10^{-11} \sqrt{T_{\text{gas}}/300}$	31 <sup>g</sup>
$\text{Ar}(2p_8) + \text{He} \leftrightarrow \text{Ar}(1s) + \text{He}$	$0.10 \times 10^{-11} \sqrt{T_{\text{gas}}/300}$	30 <sup>g,h</sup>
$\text{Ar}(2p_8) + \text{Ar} \leftrightarrow \text{Ar}(2p_9) + \text{Ar}$	$1.10 \times 10^{-11}$	30
$\text{Ar}(2p_8) + \text{He} \leftrightarrow \text{Ar}(2p_9) + \text{He}$	$4.50 \times 10^{-11}$	30
$\text{Ar}(2p_8) + \text{Ar} \leftrightarrow \text{Ar}(2p_{10}) + \text{Ar}$	$1.10 \times 10^{-11}$	30
$\text{Ar}(2p_8) + \text{He} \leftrightarrow \text{Ar}(2p_{10}) + \text{He}$	$0.40 \times 10^{-11}$	30
$\text{Ar}(2p_9) + \text{Ar} \leftrightarrow \text{Ar}(2p_{10}) + \text{Ar}$	$2.60 \times 10^{-11}$	30
$\text{Ar}(2p_9) + \text{He} \leftrightarrow \text{Ar}(2p_{10}) + \text{He}$	$1.60 \times 10^{-11}$	30
$\text{Ar}(h.l.) + \text{M} \leftrightarrow \text{Ar}(2p) + \text{M}$	$1.00 \times 10^{-11}$	25 <sup>e,i</sup>
$\text{He}^* + \text{He}^* \rightarrow \text{He}^+ + \text{He} + e^-$	$1.50 \times 10^{-9}$	32
$\text{Ar}(1s) + \text{Ar}(1s) \rightarrow \text{Ar}^+ + \text{Ar} + e^-$	$5.00 \times 10^{-10} \sqrt{T_{\text{gas}}/300}$	31
$\text{Ar}(1s) + \text{Ar}(2p) \rightarrow \text{Ar}^+ + \text{Ar} + e^-$	$5.00 \times 10^{-10} \sqrt{T_{\text{gas}}/300}$	31
$\text{Ar}(2p) + \text{Ar}(2p) \rightarrow \text{Ar}^+ + \text{Ar} + e^-$	$5.00 \times 10^{-10} \sqrt{T_{\text{gas}}/300}$	25 <sup>h</sup>
$\text{Ar}(h.l.) + \text{Ar}(1s) \rightarrow \text{Ar}^+ + \text{Ar} + e^-$	$7.00 \times 10^{-10} \sqrt{T_{\text{gas}}/300}$	31
$\text{Ar}_2^+ + \text{M} \rightarrow \text{Ar}^+ + \text{Ar} + \text{M}$	$6.10 \times 10^{-6} T_{\text{gas}}^{-1} \exp(-15,130/T_{\text{gas}})$	24 <sup>i</sup>
$\text{He}_2^+ + \text{M} \rightarrow \text{He}^+ + \text{He} + \text{M}$	$1.40 \times 10^{-6} T_{\text{gas}}^{-0.67} \exp(-28,090/T_{\text{gas}})$	24 <sup>i</sup>
$\text{HeAr}^+ + \text{Ar} \rightarrow \text{Ar}^+ + \text{He} + \text{Ar}$	$2.94 \times 10^{-11} \sqrt{T_{\text{gas}}} \exp(-298/T_{\text{gas}})$	Estimated <sup>j</sup>
$\text{HeAr}^+ + \text{He} \rightarrow \text{Ar}^+ + \text{He} + \text{He}$	$1.17 \times 10^{-11} \sqrt{T_{\text{gas}}} \exp(-298/T_{\text{gas}})$	Estimated <sup>j</sup>
$\text{Ar}_2^* + \text{Ar}_2^* \rightarrow \text{Ar}_2^+ + \text{Ar} + \text{Ar} + e^-$	$5.00 \times 10^{-10}$	33
$\text{He}_2^* + \text{He}_2^* \rightarrow \text{He}_2^+ + \text{He} + \text{He} + e^-$	$1.50 \times 10^{-9}$	23
$\text{He}^+ + \text{Ar} \rightarrow \text{He} + \text{Ar}^+$	$1.00 \times 10^{-13}$	34
$\text{He}^* + \text{Ar} \rightarrow \text{Ar}^+ + \text{He} + e^-$	$2.20 \times 10^{-11}$	35 <sup>k</sup>
$\text{He}^* + \text{Ar} \rightarrow \text{HeAr}^+ + e^-$	$4.90 \times 10^{-11}$	35 <sup>k</sup>
$\text{He}_2^+ + \text{Ar} \rightarrow \text{Ar}^+ + \text{He} + \text{He}$	$2.20 \times 10^{-10}$	36
$\text{He}_2^* + \text{Ar} \rightarrow \text{Ar}^+ + \text{He} + \text{He} + e^-$	$3.10 \times 10^{-10}$	11
<b>Three-heavy-body</b>		
$\text{Ar}^+ + \text{Ar} + \text{Ar} \rightarrow \text{Ar}_2^+ + \text{Ar}$	$2.25 \times 10^{-31} (300/T_{\text{gas}})^{0.4}$	37
$\text{Ar}^+ + \text{Ar} + \text{He} \rightarrow \text{Ar}_2^+ + \text{He}$	$1.13 \times 10^{-31} (300/T_{\text{gas}})^{0.4}$	37 <sup>l</sup>
$\text{He}^+ + \text{He} + \text{He} \rightarrow \text{He}_2^+ + \text{He}$	$0.83 \times 10^{-31} (300/T_{\text{gas}})^{0.6}$	37
$\text{He}^+ + \text{He} + \text{Ar} \rightarrow \text{He}_2^+ + \text{Ar}$	$1.66 \times 10^{-31} (300/T_{\text{gas}})^{0.6}$	37 <sup>l</sup>
$\text{He}^+ + \text{Ar} + \text{Ar} \rightarrow \text{Ar}_2^+ + \text{He}$	$1.00 \times 10^{-31}$	11
$\text{Ar}^+ + \text{He} + \text{Ar} \rightarrow \text{HeAr}^+ + \text{Ar}$	$2.50 \times 10^{-32}$	25
$\text{Ar}^+ + \text{He} + \text{He} \rightarrow \text{HeAr}^+ + \text{He}$	$1.00 \times 10^{-32}$	25
$\text{Ar}(1s_5) + \text{Ar} + \text{Ar} \rightarrow \text{Ar}_2^* + \text{Ar}$	$3.60 \times 10^{-31} T_{\text{gas}}^{-0.6}$	38
$\text{Ar}(1s_5) + \text{Ar} + \text{He} \rightarrow \text{Ar}_2^* + \text{He}$	$1.80 \times 10^{-31} T_{\text{gas}}^{-0.6}$	38 <sup>l</sup>
$\text{Ar}(1s_4) + \text{Ar} + \text{Ar} \rightarrow \text{Ar}_2^* + \text{Ar}$	$0.95 \times 10^{-32}$	38
$\text{Ar}(1s_4) + \text{Ar} + \text{He} \rightarrow \text{Ar}_2^* + \text{He}$	$0.48 \times 10^{-32}$	38 <sup>l</sup>
$\text{He}^* + \text{He} + \text{He} \rightarrow \text{He}_2^* + \text{He}$	$1.30 \times 10^{-33}$	22
$\text{He}^* + \text{He} + \text{Ar} \rightarrow \text{He}_2^* + \text{Ar}$	$2.60 \times 10^{-33}$	22 <sup>l</sup>
<b>Radiative</b>		
$\text{Ar}_2^* \rightarrow \text{Ar} + \text{Ar}$	$3.13 \times 10^5$	39
$\text{Ar}(2p_8) \rightarrow \text{Ar}(1s_4)$	$2.20 \times 10^7$	40
$\text{Ar}(2p_8) \rightarrow \text{Ar}(1s_5)$	$9.30 \times 10^6$	40
$\text{Ar}(2p_9) \rightarrow \text{Ar}(1s_5)$	$3.30 \times 10^7$	40
$\text{Ar}(2p_{10}) \rightarrow \text{Ar}(1s_4)$	$5.40 \times 10^6$	40
$\text{Ar}(2p_{10}) \rightarrow \text{Ar}(1s_5)$	$1.90 \times 10^7$	40
$\text{Ar}(1s_4) \rightarrow \text{Ar}$	$1.20 \times 10^8$	40 <sup>m</sup>
$\text{Ar}(h.l.) \rightarrow \text{Ar}$	$1.00 \times 10^8$	31
$\text{Ar}(h.l.) \rightarrow \text{Ar}(2p_{10})$	$3.00 \times 10^6$	31

TABLE II. (Continued.)

Reaction	Rate coefficient $\left[\frac{1}{s}, \frac{\text{cm}^2}{s}, \text{ or } \frac{\text{cm}^6}{s}\right]$	References
$Ar(h.l.) \rightarrow Ar(2p_9)$	$4.00 \times 10^6$	31
$Ar(h.l.) \rightarrow Ar(2p_8)$	$3.00 \times 10^6$	31
$Ar(h.l.) \rightarrow Ar(1s_5)$	$1.00 \times 10^6$	31 <sup>n</sup>
$Ar(h.l.) \rightarrow Ar(1s_4)$	$1.00 \times 10^6$	31 <sup>n</sup>

<sup>a</sup>Shifted in energy relative to the  $Ar(1s_5)$  ionization cross-section.

<sup>b</sup>The  $Ar(3d_{12})$  excitation cross-section extracted from PROGRAM MAGBOLTZ is used for  $Ar(h.l.)$ .

<sup>c</sup>Shifted in energy relative to the Ar ground state excitation to  $Ar(3d_{12})$  and used for  $Ar(h.l.)$ .

<sup>d</sup>Shifted in energy relative to the  $Ar(2p_{10})$  excitation to  $Ar(2p_8)$ .

<sup>e</sup>Following Shon and Kushner,<sup>25</sup> using a value of 1/10 times the dissociative recombination rate for  $Ar_2^+$ .

<sup>f</sup>Rate coefficient corresponds to room temperature and is larger for temperatures above 300 K.<sup>30</sup>

<sup>g</sup>Assuming equal branching.

<sup>h</sup>Assuming  $\sqrt{T_{\text{gas}}/300}$  temperature dependence following Zhu and Pu.<sup>31</sup>

<sup>i</sup>Assuming rate coefficients for He as the second body are the same as Ar as the second body.

<sup>j</sup>Calculated from the forward rate using detailed balance with the  $HeAr^+$  parameters provided by Dabrowski, Herzberg, and Yoshino.<sup>41</sup>

<sup>k</sup>Branching ratio from Shon.<sup>11</sup>

<sup>l</sup>Assuming three-body rate coefficients with He as the third body are 1/2 the rate coefficient for Ar as the third body.

<sup>m</sup>Not including radiation trapping.

<sup>n</sup>Assuming equal branching from  $Ar(3p)$ .

mixtures. The mobility of  $Ar^+$  in Ar is  $1.54 \text{ cm}^2/\text{V} \cdot \text{s}$ , in contrast to  $20.5 \text{ cm}^2/\text{V} \cdot \text{s}$  in He.<sup>47,48</sup> For a 7% Ar in He mixture, the effective mobility calculated by Blanc's law is  $11.0 \text{ cm}^2/\text{V} \cdot \text{s}$  and is used for all Ar based ions. He based ions  $He^+$  and  $He_2^+$  are assigned mobilities of  $10.7$  and  $16.2 \text{ cm}^2/\text{V} \cdot \text{s}$ , respectively, based on measurements in pure He (Ref. 49).

For reactions of the form



the system of rate equations integrated over time are described by

$$\begin{aligned} \frac{d[N_i]}{dt} &= \sum_{i=1}^{i_{\text{max}}} Q_{li}(t), \\ R_i &= k_i[A]^a[B]^b, \\ Q_{Ai} &= (a' - a)R_i, \\ Q_{Bi} &= -bR_i, \\ Q_{Ci} &= cR_i, \end{aligned} \quad (4)$$

where  $[N_i]$  is the concentration of species  $N_i$ ,  $i$  is the reaction number,  $a$ ,  $b$ ,  $c$  are the stoichiometric coefficients of the species  $A$ ,  $B$ ,  $C$  in reaction  $i$ ,  $R_i$  is the reaction rate for reaction  $i$ ,  $Q$  is the overall production/loss rate for a particular species, and  $\Delta\epsilon$  is the energy gained or lost in the reaction.<sup>44</sup> An estimated power density of  $\sim 85 \text{ W/cm}^3$  applied over the 20  $\mu\text{s}$  pulse corresponds to a gas temperature increase of approximately 10 K, and this increase in temperature is ignored for these calculations.

Voltages across the positive column are given by

$$\begin{aligned} V_{PC} &= V_{\text{external}} - I_D R - V_C, \\ &= V_{\text{electrode}} - V_C, \end{aligned} \quad (5)$$

where  $V_{PC}$  is the voltage across the positive column,  $V_{\text{external}}$  is the voltage applied by the external circuit,  $I_D$  is the

discharge current,  $R$  is a  $500 \Omega$  ballast resistor, and  $V_C$  is the cathode fall. The electrode voltage,  $V_{\text{electrode}}$ , corresponds to the voltage applied by the external circuit minus the voltage drop due to the ballast resistor. An estimated secondary emission coefficient of  $\gamma = 0.02$  for the stainless steel electrodes provides a cathode fall of approximately 160 V. Reduced electric fields in the positive column are calculated from the positive column voltage by

$$\frac{E}{N} = \frac{V_{PC}}{Nd}, \quad (6)$$

where  $d$  is the electrode separation.

## B. One-dimensional model

A fluid approach is used to model the discharge in one-dimension,<sup>50-54</sup> implemented through COMSOL Multiphysics<sup>TM</sup>. The electron density,  $n_e$ , and energy density,  $n_\epsilon$ , are calculated over time via the one-dimensional drift-diffusion equations:

$$\frac{\partial n_e}{\partial t} + \frac{\partial \Gamma_e}{\partial x} = R_e, \quad (7)$$

$$\frac{\partial n_\epsilon}{\partial t} + \frac{\partial \Gamma_\epsilon}{\partial x} + E \Gamma_e = R_\epsilon, \quad (8)$$

$$\Gamma_e = -n_e \mu_e E - \frac{\partial}{\partial x} (D_e n_e), \quad (9)$$

$$\Gamma_\epsilon = -n_\epsilon \mu_\epsilon E - \frac{\partial}{\partial x} (D_\epsilon n_\epsilon), \quad (10)$$

where the subscript  $e$  refers to the electron density, and  $\epsilon$  refers to the electron energy density. Electron mobilities,  $\mu_{e,\epsilon}$ , diffusion coefficients,  $D_{e,\epsilon}$ , and electron impact rate coefficients are calculated from BOLSIG+, and a look-up table is used to extract the values based on the local  $T_e$ . The

local electron temperature is mapped to an effective  $E/N$  from BOLSIG+, which is used to extract an EEDF for each point in space. Transport parameters and electron impact rate coefficients are calculated for each point in space from the EEDF corresponding to the local  $T_e$ . Reaction source terms are calculated from the plasma chemistry in the same manner as Eq. (4), with the addition of an energy term,  $\Delta\epsilon_i$ , in the energy source term  $R_\epsilon$  to account for the energy gained or lost from reaction  $i$ .

Ignoring neutral gas flow, heavy particle transport is calculated by

$$\frac{\partial n_k}{\partial t} + \frac{\partial \Gamma_k}{\partial x} = R_k, \quad (11)$$

$$\frac{\partial n_p}{\partial t} + \frac{\partial \Gamma_p}{\partial x} = R_p, \quad (12)$$

$$\Gamma_k = -D_k \frac{\partial n_k}{\partial x}, \quad (13)$$

$$\Gamma_p = n_p \mu_p E - D_p \frac{\partial n_p}{\partial x}, \quad (14)$$

where  $n_k$  is the density of neutral species  $k$ ,  $n_p$  is the density of ion species  $p$ ,  $D_{k,p}$  are the diffusion coefficients,  $R_{k,p}$  are the reaction source terms, and  $\mu_p$  is the ion mobility. The ion flux  $\Gamma_p$  has a drift term due to migration in the electric field,  $E = -\partial V/\partial x$ . Electric potentials are calculated from Poisson's equation

$$-\frac{\partial^2 V}{\partial x^2} = \frac{q_e}{\epsilon_0} \left( \sum_{p=1}^P n_p - n_e \right), \quad (15)$$

where all ions are assumed to be singly charged with charge  $q_e$ .

Near the electrodes, electrons are lost due to thermal motion to the surface, and electrons are created due to secondary emission from ion collisions with the surface, providing the following boundary conditions:<sup>55</sup>

$$\mathbf{n} \cdot \Gamma_e = \frac{1}{2} v_{e,th} n_e - \xi \sum_p \gamma_p \Gamma_p \cdot \mathbf{n}, \quad (16)$$

$$\mathbf{n} \cdot \Gamma_\epsilon = \frac{5}{6} v_{e,th} n_e - \xi \sum_p \epsilon_p \gamma_p \Gamma_p \cdot \mathbf{n}, \quad (17)$$

$$\xi = \begin{cases} 1, & \text{if } \Gamma_p \cdot \mathbf{n} > 0 \\ 0, & \text{otherwise} \end{cases}$$

where  $\mathbf{n}$  is the outward normal vector to the boundary (electrode),  $v_{e,th}$  is the thermal velocity of electrons,  $\epsilon_p$  is the average energy of the secondary electrons, and  $\gamma_p$  is the secondary emission coefficient for ion species  $p$ . Boundary conditions for heavy species follow

$$\mathbf{n} \cdot \Gamma_k = \frac{1}{2} v_{k,th} n_k, \quad (18)$$

$$\mathbf{n} \cdot \Gamma_p = \frac{1}{2} v_{p,th} n_p + n_p \mu_p \mathbf{E} \cdot \mathbf{n}, \quad (19)$$

where the sticking coefficient is assumed to be unity, and  $v_{k,th}$  and  $v_{p,th}$  are the thermal neutral and ion velocities, respectively.

Solutions to the system of partial differential equations are approximated over time using the Galerkin finite element method with quadratic Lagrange shape functions. An implicit backward differentiation formula is used for time stepping.

### III. SIMULATIONS

Simulations are performed for a 1000 V, 20  $\mu$ s pulse at a pressure of 270 Torr in a mixture of 7% Ar in He, similar to the experiments performed by Han *et al.*<sup>10</sup> A comparison between the zero and one-dimensional models is performed over time by selecting a representative position in the positive column of the one-dimensional model, here taken to be 3.5 mm from the cathode. Results from the one-dimensional model at the 3.5 mm position are then compared to the zero-dimensional model over time.

Voltages, electron temperatures, reduced electric fields, and current densities simulated by the models show excellent agreement over time in the positive column (Fig. 2). During breakdown, the electron density increases and current begins to flow. As the current flows across the ballast resistor the electrode voltage,  $V_{electrode}$ , is reduced from 1000 V to approximately 400 V. This decrease in  $V_{electrode}$  in combination with the formation of a cathode fall reduces the positive column  $E/N$  from the peak value of 23 Td during breakdown to 4–5 Td post-breakdown. Similarly, the positive column  $T_e$  experiences a reduction from approximately 4 eV to 2 eV due to the reduction in  $E/N$ . After pulse termination, the electron temperature rapidly approaches the neutral gas temperature.

Electron densities in the positive column show a rapid increase during breakdown, followed by an almost constant magnitude during the remainder of the pulse, as shown in Fig. 3. Initially,  $Ar^+$  is the dominant ion, but three-body collisions at atmospheric pressures convert  $Ar^+$  to  $HeAr^+$  and  $Ar_2^+$  throughout the pulse duration. The  $\sim 0.02$  eV binding energy of  $HeAr^+$  allows for rapid dissociation due to neutral collisions,  $HeAr^+ + M \rightarrow Ar^+ + He + M$ , and yields a positive column  $HeAr^+$  density of approximately  $10^9 \text{ cm}^{-3}$ . The  $\sim 1.26$  eV binding energy of  $Ar_2^+$  yields dissociation rates

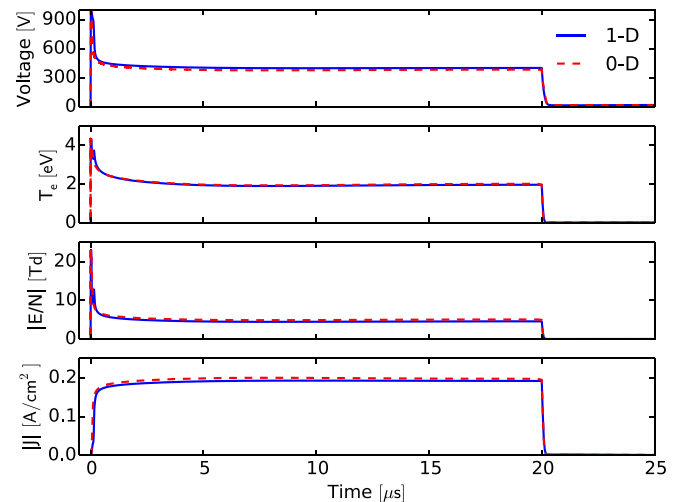


FIG. 2. Electrode voltage, positive column  $T_e$ ,  $E/N$  magnitude, and current density magnitude over time for the 20  $\mu$ s pulse.



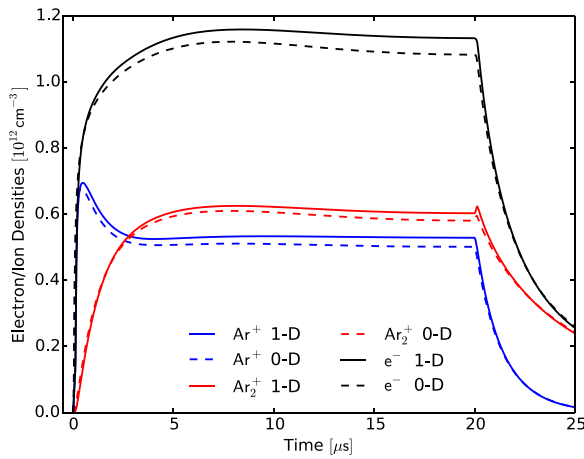


FIG. 3. Positive column electron and ion densities over time for the 20 μs pulse. The HeAr<sup>+</sup> densities are too low (~10<sup>9</sup> cm<sup>-3</sup>) to appear on this scale.

due to neutral collisions,  $Ar_2^+ + M \rightarrow Ar^+ + Ar + M$ , that are insignificant at 300 K. As a result, Ar<sub>2</sub><sup>+</sup> quickly becomes the dominant ion with a positive column density of  $\sim 6 \times 10^{11}$  cm<sup>-3</sup> also displayed in Fig. 3.

After pulse termination, electron and ion densities decay rapidly due to the removal of the large voltage required to sustain the glow discharge. The one- and zero-dimensional models show reasonable agreement throughout the pulse duration, with slightly lower electron densities predicted by the zero-dimensional model. Both models predict a temporal variation in electron and ion densities before pulse termination, indicating that a steady-state was not reached over the pulse duration.

Excited species densities show peaks during breakdown followed by a decay throughout the remainder of the pulse (Fig. 4), qualitatively matching the Ar(1s<sub>5</sub>) absorption and Ar(2p<sub>10</sub>) fluorescence measurements by Han *et al.*<sup>10</sup> Densities of the Ar(1s) species show a smooth decay, while the Ar(2p) species show a large initial spike. This behavior is due to electron excitation from ground state following  $Ar + e^- \rightarrow Ar^* + e^-$ , where excitation to the Ar(1s) manifold is maintained at

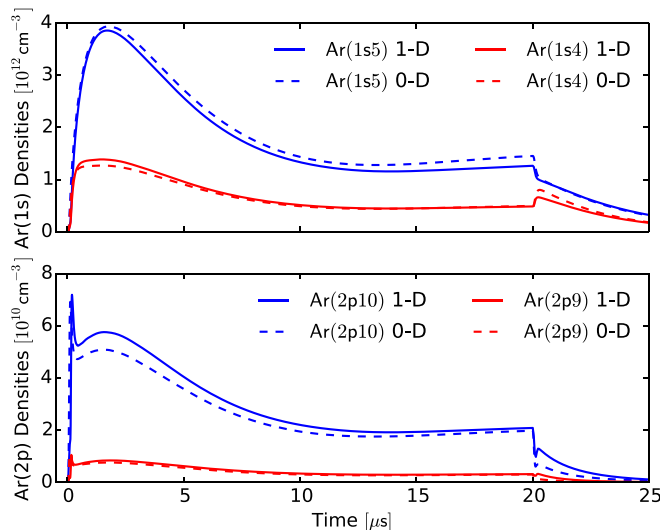


FIG. 4. Positive column Ar(1s) and Ar(2p) densities over time for the 20 μs pulse. The Ar(2p<sub>8</sub>) densities (not shown) are nearly the same as the Ar(2p<sub>9</sub>) densities.

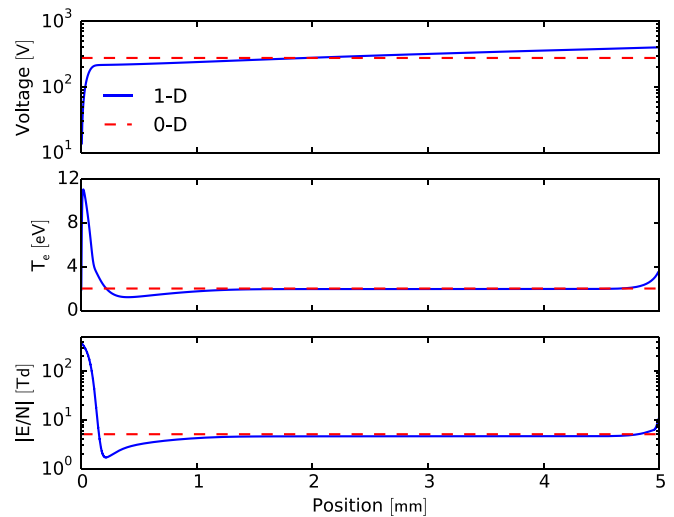


FIG. 5. Spatial profile of voltage,  $T_e$ , and  $E/N$  magnitude at the end of the 20 μs pulse.

the post-breakdown  $E/N$  magnitudes, while Ar(2p) manifold excitation is drastically reduced after breakdown. The zero- and one-dimensional simulations are in agreement throughout the pulse and after pulse termination.

Spatial distributions are analyzed at the end of the pulse (20 μs), as the discharge approaches a steady-state. In the one-dimensional model, the cathode is located at  $x=0$  mm with the anode at  $x=5$  mm. Voltage,  $T_e$ , and  $E/N$  show agreement between the zero- and one-dimensional models in the positive column (Fig. 5). As expected, a large voltage drop of  $\sim 215$  V is observed near the cathode, giving rise to a large  $E/N$  magnitude, which in turn elevates the local  $T_e$ . An  $E/N$  magnitude of approximately 380 Td gives rise to a  $T_e$  of 11 eV near the cathode. A positive column  $E/N$  magnitude of 4–5 Td produces an electron temperature of approximately 2 eV. Near the anode, a slight increase in  $E/N$  magnitude and  $T_e$  is observed due to a voltage drop of approximately 3 V occurring over  $\sim 30$  μm.

Figure 6 displays electron and ion densities versus position near the end of the pulse and shows agreement between

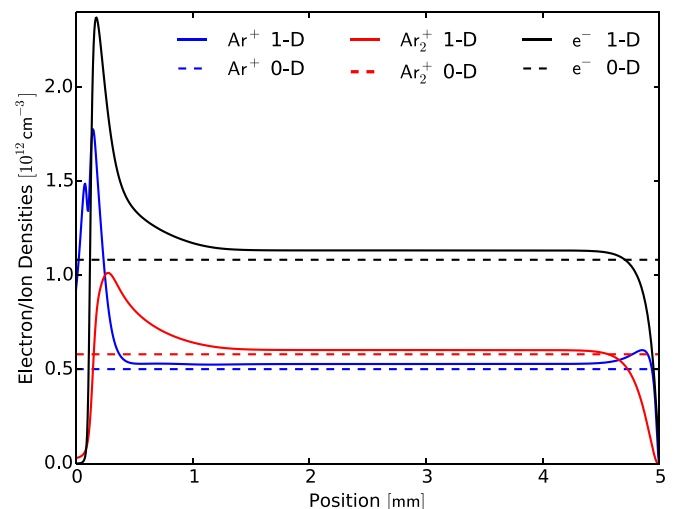


FIG. 6. Spatial profile of electron and ion densities at the end of the 20 μs pulse.

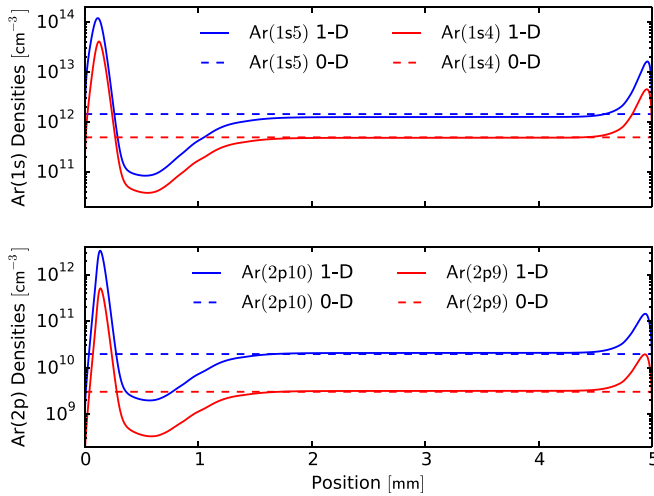


FIG. 7. Spatial profile of  $Ar(1s)$  and  $Ar(2p)$  densities at the end of the 20  $\mu s$  pulse.

the zero- and one-dimensional models in the positive column. Peak  $Ar^+$  and electron densities are observed in the cathode layer due to ionization rate dependence on  $E/N$ . In the positive column,  $Ar_2^+$  is the dominant ion with densities  $\sim 15\%$  larger than  $Ar^+$ . However,  $Ar^+$  is the dominant ion near the electrodes. The low binding energy of  $HeAr^+$  together with the reaction  $HeAr^+ + M \rightarrow Ar^+ + He + M$  yields  $HeAr^+$  densities of  $\sim 10^{11} \text{ cm}^{-3}$  in the cathode layer and  $\sim 10^9 \text{ cm}^{-3}$  elsewhere in the cavity.

Similarly, excited species densities simulated by the two models are nearly equal in the positive column (Fig. 7). Peak densities are observed in the cathode layer where  $E/N$  and  $T_e$  are elevated, increasing the excitation rates. Excitation rates are also increased near the anode due to the increase in  $E/N$  magnitude and  $T_e$ . This spatial information is vital to operation of an OPRGL, due to the dependence of laser intensity on the metastable density. The measured distribution of laser intensity was found to follow a similar pattern,<sup>10</sup> with a large peak in intensity near the cathode. However, the measured peak was found to take place approximately 1 mm from the cathode, while the simulations show the peak 0.1 mm from the cathode. This difference is most likely due to the non-local ionization/excitation behavior in the cathode layer and negative glow, which is underestimated using fluid approximations.<sup>56,57</sup> A hybrid kinetic-fluid model would provide more insight into the electron behavior near the electrodes.

#### IV. KINETICS

Plasma kinetics are analyzed for the zero-dimensional model by investigating production and loss rates over time. The dominant electron production mechanism during breakdown is ionization from the ground state,  $Ar + e^- \rightarrow Ar^+ + 2e^-$  (Fig. 8). After breakdown, with the reduction in  $E/N$  and an increase in  $Ar_2^+$  density, the dominant production rate becomes excimer ionization:  $Ar_2^* + e^- \rightarrow Ar_2^+ + 2e^-$ . Throughout the simulation, dissociative recombination of  $Ar_2^+$  is the dominant electron loss mechanism, followed by ambipolar diffusion. A large change occurs in the loss rates after pulse termination due to the ambipolar diffusion and

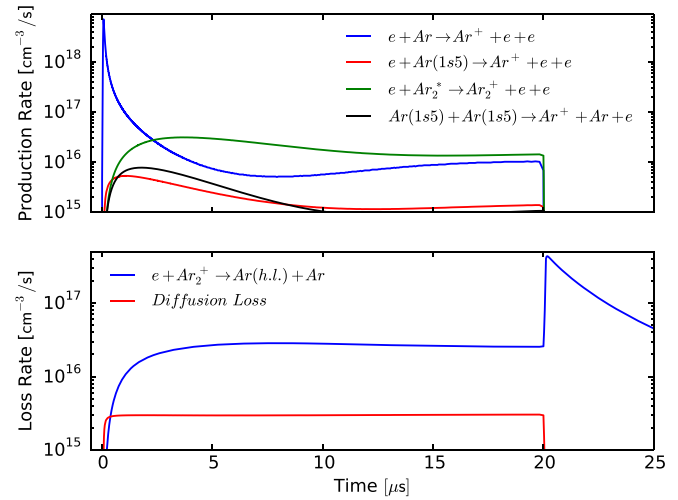


FIG. 8. Positive column electron production and loss rates over time. The large increase in the dissociative recombination rate after pulse termination is caused by a large decrease in  $T_e$  due to the removal of the applied electric field.

dissociative recombination dependence on  $T_e$ . Once the external voltage is reduced,  $T_e$  experiences a large decrease, which decreases the ambipolar diffusion rate and increases the dissociative recombination rate.

Similar to the electron rates, the dominant  $Ar(1s_5)$  production mechanism during breakdown is due to excitation from the ground state,  $Ar + e^- \rightarrow Ar(1s_5) + e^-$  (Fig. 9). After breakdown, the majority of  $Ar(1s_5)$  is produced by electron or neutral de-excitation from  $Ar(1s_4)$ . The dominant loss rate, over all times, is due to electron excitation to  $Ar(1s_4)$ . However, superelastic collisions reduce the overall loss rate of  $Ar(1s_5)$ . After pulse termination, the large decrease in  $T_e$  causes an increase in the  $Ar(1s_5) + e^- \leftrightarrow Ar(1s_4) + e^-$  rates due to a collapse in the EEDF towards lower energies and the relatively small energy difference between the  $Ar(1s_5)$  and  $Ar(1s_4)$  levels ( $\sim 0.08 \text{ eV}$ ).

Electron excitation of ground state Ar to  $Ar(2p_9)$  shows a spike during breakdown, when  $E/N$  is large, followed by a decrease post breakdown (Fig. 10). After breakdown, the

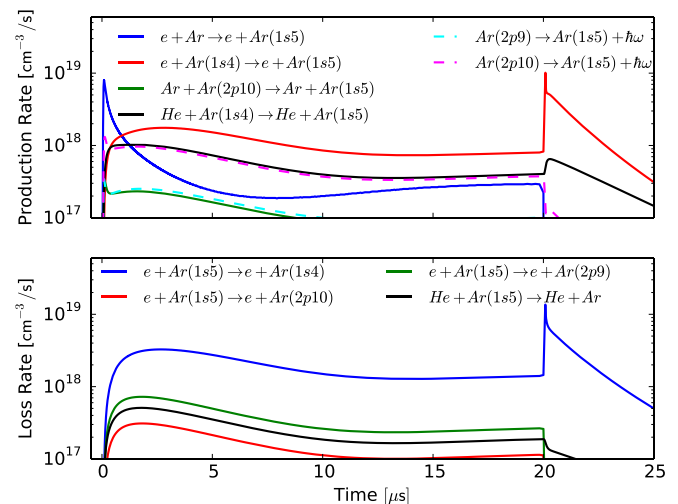


FIG. 9. Positive column  $Ar(1s_5)$  production and loss rates over time. After pulse termination, the decrease in  $T_e$  causes a collapse in the EEDF towards lower energies, which increases  $Ar(1s_5) + e^- \leftrightarrow Ar(1s_4) + e^-$  rates.

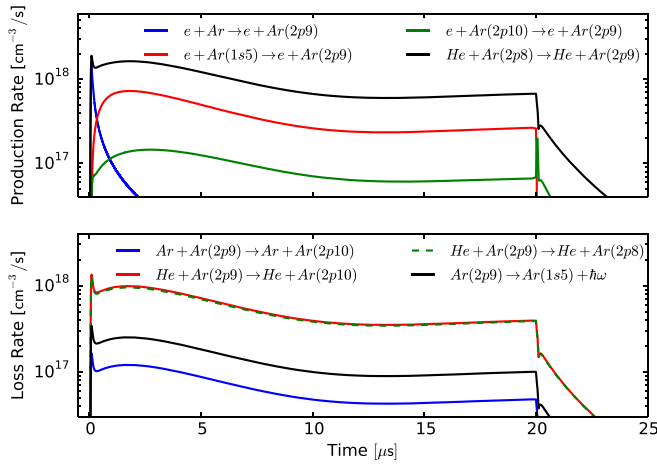


FIG. 10. Positive column  $Ar(2p_9)$  production and loss rates over time. The post-pulse He mixing rates follow the simulated  $Ar(2p)$  densities (using the zero-dimensional model), which show a large decrease at pulse termination followed by a steady decay. After pulse termination, the decrease in  $T_e$  causes a collapse in the EEDF towards lower energies, which increases the  $Ar(2p_{10}) + e^- \rightarrow Ar(2p_9) + e^-$  rate.

majority of  $Ar(2p_9)$  is produced through He collisions with  $Ar(2p_8)$  and electron excitation from  $Ar(1s_5)$ . An important mechanism to OPRGL performance is collisional mixing of  $Ar(2p)$  levels which is required to transfer pumped  $Ar(2p_9)$  densities to  $Ar(2p_{10})$ . For the 7% Ar in He mixture, collisions with He are the dominant mixing mechanism, with almost equal rates to  $Ar(2p_{10})$  and  $Ar(2p_8)$ . At 300 K, the rate coefficients for  $Ar(2p_9) + He \rightarrow Ar(2p_{10}/2p_8) + He$  are in the range of  $1.5 - 1.6 \times 10^{-11} \text{ cm}^3/\text{s}$ , with the rate to  $Ar(2p_{10})$  slightly larger than the rate to  $Ar(2p_8)$ . This indicates that a roughly equal number of optically pumped  $Ar(2p_9)$  atoms will collisionally transition to the  $Ar(2p_{10})$  and  $Ar(2p_8)$ .

While the rate information by itself is useful, it does not provide enough information to form a complete picture due to the dependence of the rates on intermediate species densities. To analyze the principal pathways, PumpKin (Pathway reduction Method for Plasma KINetic models) is employed.<sup>58</sup> PumpKin calculates the principal pathways by

using an algorithm based on branching at “fast” species. The fast species are identified as species with a short lifetime relative to the other species. This algorithm determines the sequences of reactions responsible for creating and destroying a species of interest.

Applying PumpKin to the entire pulse period provides pathways matching the dominant rates discussed above and also presents additional information about the reagents/products involved with the reactions (Table III). For example, the dominant electron loss pathway is due to dissociative recombination via  $Ar_2^+ + e^- \rightarrow Ar(h.l.) + Ar$  followed by radiation to the ground state:  $Ar(h.l.) \rightarrow Ar + \hbar\omega$ . The dominant electron production pathway early in the pulse is due to ionization of Ar, which occurs during breakdown. Ionization of  $Ar_2^*$  through  $Ar_2^* + e^- \rightarrow Ar_2^+ + 2e^-$  is the dominant pathway after breakdown.

Concerning metastable production, the dominant pathway is simply electron excitation from the ground state. The second largest production pathway is due to electron excitation to  $Ar(1s_4)$  followed by electron de-excitation through  $Ar(1s_4) + e^- \rightarrow Ar(1s_5) + e^-$ . Loss pathways include electron excitation from  $Ar(1s_5)$  to  $Ar(1s_4)$  followed by radiation to the ground state:  $Ar(1s_4) \rightarrow Ar + \hbar\omega$ . Neutral quenching by He,  $Ar(1s_5) + He \rightarrow Ar + He$ , is the second largest loss pathway. The importance of radiation trapping becomes apparent due to the loss mechanism involving radiation from  $Ar(1s_4)$ . Radiation from  $Ar(1s_4)$  acts as a sink for the metastable density, and a lowered effective radiation rate due to radiation trapping results in elevated concentrations of  $Ar(1s_5)$ .

Production pathways for  $Ar(2p_9)$  are dominated by electron excitation from the  $Ar(1s)$  manifold, either directly from  $Ar(1s_5)$  or through  $Ar(1s_4)$ . Dominant loss pathways for  $Ar(2p_9)$  are primarily through collisions with He to  $Ar(2p_{10})$  followed by radiation to  $Ar(1s_5)$ , or by radiation directly to  $Ar(1s_5)$ .

## V. CONCLUSIONS

Simulations of a 7% Ar in He pulsed DC discharge at a pressure of 270 Torr are performed for a 20  $\mu\text{s}$ , 1000 V pulse

TABLE III. Electron,  $Ar(1s_5)$ , and  $Ar(2p_9)$  principal pathways calculated by PumpKin over the entire pulse period. The pathways are in order by magnitude (larger rates first), and the arrows,  $\Rightarrow$ , link the sequential reactions.

Species	Production or loss	Principal pathway
$e^-$	Production	(1) $Ar + e^- \rightarrow Ar^+ + 2e^-$ (2) $Ar_2^* + e^- \rightarrow Ar_2^+ + 2e^-$
	Loss	(1) $Ar_2^+ + e^- \rightarrow Ar(h.l.) + Ar \Rightarrow Ar(h.l.) \rightarrow Ar + \hbar\omega$ (2) Ambipolar diffusion
$Ar(1s_5)$	Production	(1) $Ar + e^- \rightarrow Ar(1s_5) + e^-$ (2) $Ar + e^- \rightarrow Ar(1s_4) + e^- \Rightarrow Ar(1s_4) + e^- \rightarrow Ar(1s_5) + e^-$
	Loss	(1) $Ar(1s_5) + e^- \rightarrow Ar(1s_4) + e^- \Rightarrow Ar(1s_4) \rightarrow Ar + \hbar\omega$ (2) $Ar(1s_5) + He \rightarrow Ar + He$
$Ar(2p_9)$	Production	(1) $Ar(1s_5) + e^- \rightarrow Ar(2p_9) + e^-$ (2) $Ar(1s_5) + e^- \rightarrow Ar(1s_4) + e^- \Rightarrow Ar(1s_4) + e^- \rightarrow Ar(2p_8) + e^- \Rightarrow Ar(2p_8) + He \rightarrow Ar(2p_9) + He$
	Loss	(1) $Ar(2p_9) + He \rightarrow Ar(2p_{10}) + He \Rightarrow Ar(2p_{10}) \rightarrow Ar(1s_5) + \hbar\omega$ (2) $Ar(2p_9) \rightarrow Ar(1s_5) + \hbar\omega$

using both a zero-dimensional model of the positive column and a one-dimensional fluid model. Species relevant to the operation of an optically pumped rare-gas laser are analyzed over a single pulse duration to identify key kinetic pathways. Comparisons of the two models show agreement in the positive column, where the zero-dimensional model is appropriate. Both models predict a spike in excitation and ionization rates during breakdown due to elevated voltage,  $E/N$  magnitude, and  $T_e$  during pulse initiation. After breakdown, the combination of a reduced electrode voltage and cathode fall formation results in a factor of 5 decrease in the positive column  $E/N$ . This reduction in  $E/N$  drastically decreases Ar excitation and ionization via electron impact, with an order of magnitude reduction in excitation rates and a two order of magnitude reduction in ionization rate within 2  $\mu$ s after breakdown.

Electron densities steadily approach a constant value, while the dominant ion shifts from  $Ar^+$  to  $Ar_2^+$  over the pulse duration due to three-body collisions. For the geometry and simulated discharge conditions, the dissociative recombination was found to be the dominant electron loss mechanism. Metastable loss rates rapidly increase post-breakdown, resulting in peak metastable densities near  $4 \times 10^{12} \text{ cm}^{-3}$ , decreasing by a factor of 3 over the pulse duration. Radiation trapping was found to play a key role in metastable decay rates through the reaction sequence  $Ar(1s_5) + e^- \rightarrow Ar(1s_4) + e^-$  followed by  $Ar(1s_4) \rightarrow Ar + \hbar\omega$ . The  $Ar(2p)$  species display initial spikes followed by an immediate reduction in density after breakdown due to the reduced electron excitation rates from ground state at the post-breakdown  $E/N$ . Collisions with He are observed to be responsible for  $Ar(2p_9)$  loss, with an almost equal transfer to the  $Ar(2p_{10})$  and  $Ar(2p_8)$  levels. As expected, excited species densities are largest near the cathode layer, with a two order of magnitude difference between the peak and positive column densities.

Finally, we note that metastable  $Ar(1s_5)$  densities are highly dependent on the reduced electric field,  $E/N$ . Furthermore, the laser performance also depends strongly on  $Ar(1s_5)$  densities. As a result, efforts to maintain an elevated  $E/N$  over large active volumes will be helpful in OPRGL development.

## ACKNOWLEDGMENTS

This work was supported by the High Energy Laser Joint Technology Office. We would like to thank Michael Heaven, Jiande Han, and William Bailey for several useful discussions. Also, we would like to thank Leanne Pitchford for her help tracking down some of the reaction rate coefficients. Finally, we would like to thank the Department of Defense Supercomputing Resource Center for the use of their resources.

- <sup>1</sup>J. Han, L. Glebov, G. Venus, and M. C. Heaven, *Opt. Lett.* **38**, 5458 (2013).
- <sup>2</sup>W. Rawlins, K. Galbally-Kinney, S. Davis, A. Hoskinson, J. Hopwood, and M. Heaven, *Opt. Express* **23**, 4804 (2015).
- <sup>3</sup>A. Demyanov, I. Kochetov, and P. Mikheyev, *J. Phys. D: Appl. Phys.* **46**, 375202 (2013).

- <sup>4</sup>J. Han, M. C. Heaven, G. D. Hager, G. B. Venus, and L. B. Glebov, *Proc. SPIE* **8962**, 896202 (2014).
- <sup>5</sup>Y. P. Raizer, *Gas Discharge Physics* (Springer Berlin, 1997), Vol. 2.
- <sup>6</sup>S. Ashida, C. Lee, and M. Lieberman, *J. Vac. Sci. Technol. A* **13**, 2498 (1995).
- <sup>7</sup>M. A. Lieberman and A. J. Lichtenberg, *Principles of Plasma Discharges and Materials Processing*, 2nd ed. (Wiley, Hoboken, New Jersey, 2005).
- <sup>8</sup>Z. Yang, G. Yu, H. Wang, Q. Lu, and X. Xu, *Opt. Express* **23**, 13823 (2015).
- <sup>9</sup>A. R. Hoskinson, J. Gregório, J. Hopwood, K. Galbally-Kinney, S. J. Davis, and W. T. Rawlins, *J. Appl. Phys.* **119**, 233301 (2016).
- <sup>10</sup>J. Han, M. C. Heaven, D. Emmons, G. P. Perram, D. E. Weeks, and W. F. Bailey, *Proc. SPIE* **9729**, 97290D (2016).
- <sup>11</sup>J. W. Shon, "Modeling of high-pressure rare gas lasers: Kinetics and plasma chemistry," Ph.D. thesis (University of Illinois at Urbana-Champaign, 1993).
- <sup>12</sup>G. Hagelaar and L. Pitchford, *Plasma Sources Sci. Technol.* **14**, 722 (2005).
- <sup>13</sup>A. V. Phelps, see <http://jilawww.colorado.edu/avp/> for Phelps database, 2008.
- <sup>14</sup>S. F. Biagi, see nl.lxcat.net for Program magboltz, version 8.97, 2011.
- <sup>15</sup>A. Stauffer, see nl.lxcat.net for Ngfrsrdw database, York University, 2014.
- <sup>16</sup>D. Rapp and P. Englander-Golden, *J. Chem. Phys.* **43**, 1464 (1965).
- <sup>17</sup>H. Maier-Leibnitz, *Z. Phys.* **95**, 499 (1935).
- <sup>18</sup>K. McCann, M. Flannery, and A. Hazi, *Appl. Phys. Lett.* **34**, 543 (1979).
- <sup>19</sup>J. Gregório, P. Leprince, C. Boisse-Laporte, and L. Alves, *Plasma Sources Sci. Technol.* **21**, 015013 (2012).
- <sup>20</sup>S. Neeser, T. Kunz, and H. Langhoff, *J. Phys. D: Appl. Phys.* **30**, 1489 (1997).
- <sup>21</sup>A. Bultel, B. Van Ootegem, A. Bourdon, and P. Vervisch, *Phys. Rev. E* **65**, 046406 (2002).
- <sup>22</sup>S. Rauf and M. J. Kushner, *J. Appl. Phys.* **85**, 3460 (1999).
- <sup>23</sup>R. Deloche, P. Monchicourt, M. Cheret, and F. Lambert, *Phys. Rev. A* **13**, 1140 (1976).
- <sup>24</sup>J. Jonkers, M. van de Sande, A. Sola, A. Gamero, A. Rodero, and J. van der Mullen, *Plasma Sources Sci. Technol.* **12**, 464 (2003).
- <sup>25</sup>J. W. Shon and M. J. Kushner, *J. Appl. Phys.* **75**, 1883 (1994).
- <sup>26</sup>G. Bekefi, *New York* (Wiley-Interscience, 1976), Vol. 712, p. 1.
- <sup>27</sup>F. Mehr and M. A. Biondi, *Phys. Rev.* **176**, 322 (1968).
- <sup>28</sup>K. Tachibana, *Phys. Rev. A* **34**, 1007 (1986).
- <sup>29</sup>J. Han and M. Heaven, personal communication (2016).
- <sup>30</sup>J. Han and M. C. Heaven, *Opt. Lett.* **39**, 6541 (2014).
- <sup>31</sup>X.-M. Zhu and Y.-K. Pu, *J. Phys. D: Appl. Phys.* **43**, 015204 (2010).
- <sup>32</sup>F. Emmert, H. Angermann, R. Dux, and H. Langhoff, *J. Phys. D: Appl. Phys.* **21**, 667 (1988).
- <sup>33</sup>F. Kannari, M. Obara, and T. Fujioka, *J. Appl. Phys.* **57**, 4309 (1985).
- <sup>34</sup>R. Johnsen, M. Leu, and M. A. Biondi, *Phys. Rev. A* **8**, 1808 (1973).
- <sup>35</sup>W. Lindinger, A. Schmeltekopf, and F. Fehsenfeld, *J. Chem. Phys.* **61**, 2890 (1974).
- <sup>36</sup>F. Lee, C. Collins, and R. Waller, *J. Chem. Phys.* **65**, 1605 (1976).
- <sup>37</sup>J. Jones, D. Lister, D. Wareing, and N. Twiddy, *J. Phys. B: At. Mol. Phys.* **13**, 3247 (1980).
- <sup>38</sup>W. Wieme and J. Lenaerts, *J. Chem. Phys.* **74**, 483 (1981).
- <sup>39</sup>M. Rolin, S. Shabunya, J. Rostaing, and J. Perrin, *Plasma Sources Sci. Technol.* **16**, 480 (2007).
- <sup>40</sup>A. Kramida, Y. Ralchenko, J. Reader, and NIST ASD Team, see <http://physics.nist.gov/asd> for NIST atomic spectra database (ver. 5.3), 2015.
- <sup>41</sup>I. Dabrowski, G. Herzberg, and K. Yoshino, *J. Mol. Spectrosc.* **89**, 491 (1981).
- <sup>42</sup>I. Stefanović, T. Kuschel, S. Schröter, and M. Böke, *J. Appl. Phys.* **116**, 113302 (2014).
- <sup>43</sup>T. Holstein, *Phys. Rev.* **72**, 1212 (1947).
- <sup>44</sup>S. Pancheshnyi, B. Eismann, G. Hagelaar, and L. Pitchford, see <http://www.zdplaskin.laplace.univ-tlse.fr> for Computer code ZDPlasKin, University of Toulouse, LAPLACE, CNRS-UPS-INP, Toulouse, France (2008).
- <sup>45</sup>B. Eismann, "Etude numérique et théorique des phénomènes liés aux hautes pressions dans les microdécharges," Ph.D. thesis (Université de Toulouse, Université Toulouse III-Paul Sabatier, 2011).
- <sup>46</sup>M. A. Biondi and L. M. Chanin, *Phys. Rev.* **122**, 843 (1961).
- <sup>47</sup>J. Madson and H. Oskam, *Phys. Lett. A* **25**, 407 (1967).
- <sup>48</sup>W. Lindinger and D. Albritton, *J. Chem. Phys.* **62**, 3517 (1975).
- <sup>49</sup>H. Oskam and V. Mittelstadt, *Phys. Rev.* **132**, 1435 (1963).
- <sup>50</sup>D. P. Lymberopoulos and D. J. Economou, *J. Appl. Phys.* **73**, 3668 (1993).

- <sup>51</sup>J. Boeuf and L. Pitchford, *Phys. Rev. E* **51**, 1376 (1995).
- <sup>52</sup>T. Farouk, B. Farouk, D. Staack, A. Gutsol, and A. Fridman, *Plasma Sources Sci. Technol.* **15**, 676 (2006).
- <sup>53</sup>E. Gogolides and H. H. Sawin, *J. Appl. Phys.* **72**, 3971 (1992).
- <sup>54</sup>*Plasma Module User's Guide*, COMSOL Multiphysics™ v. 5.2a, Stockholm, Sweden (2016).
- <sup>55</sup>G. Hagelaar, F. D. Hoog, and G. Kroesen, *Phys. Rev. E* **62**, 1452 (2000).
- <sup>56</sup>A. Fiala, L. Pitchford, and J. Boeuf, *Phys. Rev. E* **49**, 5607 (1994).
- <sup>57</sup>D. P. Lymberopoulos and D. J. Economou, *J. Phys. D: Appl. Phys.* **28**, 727 (1995).
- <sup>58</sup>A. H. Markosyan, A. Luque, F. J. Gordillo-Vázquez, and U. Ebert, *Comput. Phys. Commun.* **185**, 2697 (2014).